MOF-derived Hierarchical Hollow NiRu-C Nanohybrid for Efficient Hydrogen Evolution Reaction①

WU Yu-Lin[a, b] XIE Ning[a, b] LI Xiao-Fang[b②]
FU Zhao-Ming[e②] WU Xin-Tao[b, c, d] ZHU Qi-Long[b, c, d②]

[a] (*College of Chemistry, Fuzhou University, Fuzhou* 350108, *China*)

[b] (*State Key Laboratory of Structural Chemistry, Fujian Institute of Research on the Structure of Matter, Chinese Academy of Sciences, Fuzhou* 350002, *China*)

[c] (*Fujian Science & Technology Innovation Laboratory for Optoelectronic Information of China, Fuzhou* 350108, *China*)

[d] (*University of Chinese Academy of Sciences, Beijing* 100049, *China*)

[e] (*Physics and Electronic Information College, Yunnan Normal University, Kunming* 650500, *China*)

ABSTRACT Designing efficient electrocatalysts for efficient hydrogen evolution is extremely desired but challenging. Herein, we report a facile MOF-assisted strategy to synthesize the hierarchical hollow spherical NiRu-C nanohybrid with closely packed rod-like bulges on the surface. Benefited from the more exposed active sites of NiRu-C nanohybrid and the efficient electron/mass transport in its unique hierarchical hollow spherical nanostructure, the optimized nanohybrid showed excellent performance for alkaline hydrogen evolution with ultralow overpotentials, which are much superior to those of Pt/C and the overwhelming majority of reported electrocatalysts. The interpretation of the reaction mechanism was further discussed with DFT calculations. Our research may provide a guidance for the development of advanced electrocatalysts with controlled morphology and excellent performance for future energy applications.

Keywords: hydrogen evolution reaction, NiRu, hollow spherical nanostructure, electrocatalysis;
DOI: 10.14102/j.cnki.0254-5861.2011-3153

1 INTRODUCTION

With the exhaustion of fossil fuels and the severe consequence of environmental contamination, the development of sustainable and green resources is exceptionally urgent[1-4]. Hydrogen possesses the merits of non-pollution, renewability and high calories, which is widely regarded as a promising resource to alleviate the energy crisis[5-7]. Hydrogen evolution reaction (HER) through electrochemical water splitting with renewable energy (*e.g.*, solar and wind energy) as power is an industrializable technique to produce high-purity hydrogen[8-12]. Up to now, the noble-metal-based materials are still needed, such as platinum/carbon (Pt/C), to deliver the high current densities with low overpotentials for HER[13]. However, the scarce reserves, high cost and poor stability greatly limit their practical applications. It is highly desirable to realize the efficient hydrogen evolution based on earth-abundant electrocatalysts, especially those showing high activity for HER[14-18].

Transition-metal-based catalysts, particularly the Ni-based catalysts with good durability and low cost, have proven to be universal and competitive electrocatalysts for various electrochemical reactions, which sheds light on the developing efficient catalysts for HER[19]. Nevertheless, the pure Ni-based catalysts are usually unable to meet the requirement in terms of activity to replace the Pt-based catalysts, especially for HER due to the weak binding interactions between Ni and hydrogen. The past endeavor has shown that alloying noble metals with Ni, even with the amount of noble metals lower by an order of magnitude, is an

Received 2 February 2021; accepted 31 March 2021

① This research was supported by the One Thousand Young Talents Program under the Recruitment Program of Global Experts, the National Natural Science Foundation of China (NSFC) (21901246 and 21905279), and the Natural Science Foundation of Fujian Province (2020J01116 and 2019J05158)

② Corresponding authors. E-mails: lixiaofang@fjirsm.ac.cn (X. Li), fuzhm1979@163.com (Z. Fu) and qlzhu@fjirsm.ac.cn (Q. L. Zhu)

effective route to modify the chemical properties of Ni-based catalysts with good balance between cost and efficiency[20]. Among noble metals, Ru shows a more economic advantage with much lower cost than Pt. Although Ru exhibits the stronger bonding strength with hydrogen, the energy barrier of water dissociation is much less than that over Pt, which has aroused widespread attention over Ru-based catalysts towards alkaline HER[21]. Therefore, the alloying of Ni and Ru can not only result in a relatively moderate metal-hydrogen bonding energy through a balance effect and accelerated water dissociation for efficient alkaline HER, but also cut down the dosage of noble metals for large-scale applications. Furthermore, the activity of NiRu alloy is also highly relevant to their nanostructures, such as the morphology and dispersion state. Often, severe agglomeration of NiRu alloy leads to the burying of surface active sites and a deterioration in its catalytic performance. Carbon supports with good stability, high conductivity and confinement effect are widely used to construct unique nanostructures, which can not only make the NiRu alloy evenly dispersed but also improve the catalytic performance[22].

As a kind of crystalline porous materials with periodic network structures formed by self-assembly of transition metal ions and organic ligands, metal-organic frameworks (MOFs) have been extremely widespread as the precursors for the controllable preparation of carbon supported metal-based nanomaterial. As a kind of crystalline porous materials with periodic network structures formed by self-assembly of transition metal ions and organic ligands, metal-organic frameworks (MOFs) have been extremely widespread as the precursors for the controllable preparation of carbon supported metal-based nanomaterials[23-25]. Furthermore, benefited from the tunability of MOFs, the postsynthetic modification of MOFs is capable of resulting into novel multicompositional MOF-based analogues, which can be used to construct unique nanostructures with designable composition, exhibiting the superiority in facilitating the structural engineering[26, 27]. Herein, inspired by the above advantages, a nanohybrid with NiRu alloy nanoparticles (NPs) supported in the hierarchical hollow spherical carbon ($NiRu_{0.06}$-C) was designed and synthesized by using a hollow spherical Ru^{3+}-doped nickel-based MOF as the starting materials, followed by the pyrolysis under inert atmosphere. The $NiRu_{0.06}$-C nanohybrid maintained the pristine hollow spherical structure with lots of rod-like bulges on the surface, where the NiRu alloy NPs with a low Ru content are homogeneously dispersed. By virtue of the unique hierarchical hollow spherical nanostructure, the $NiRu_{0.06}$-C nanohybrid showed an excellent performance towards alkaline HER with ultralow overpotentials, ranking top of the majority of the state-of-the-art catalysts. DFT calculations were further conducted to unveil the reaction mechanism. Our research may provide a guidance for the development of advanced electrocatalysts with controlled morphology and excellent performance for future energy applications.

2 EXPERIMENTAL

2. 1 Materials and characterization

The PXRD measurements were performed on a Miniflex 600 Benchtop X-ray diffractometer at 40 kV with Cu$K\alpha$ radiation to analyze crystal phases of the as-synthesized products. The SEM images were obtained at the accelerating voltage of 5 kV by a JEOL JSM6700-F instrument. The TEM and HRTEM images were recorded at the accelerating voltage of 200 kV by the FEI Tenia F20 instrument. The XPS data with monochromatic Al$K\alpha$ radiation were tested by a Thermo Fischer ESCALAB 250Xi X-ray photoelectron spectrometer ($h\nu$ = 1486.2 eV). Raman spectra were recorded on a Labram HR800 Renishaw in Via system (Horiba) by using a 532 nm laser.

2. 2 Electrocatalytic HER measurements

The catalyst ink was prepared by mixing H_2O (0.7 mL), EtOH (0.2 mL), nafion solution (0.1 mL, 5 wt% in isopropanol) and catalyst (5.0 mg) together, followed by ultrasonication for 2 h. Then, the ink (6 μL) was uniformly loaded onto a freshly polished glassy-carbon electrode (diameter = 3.0 mm) as the working electrode with a loading of 0.4 mg·cm^{-2} catalyst. The electrochemical measurements were performed at a CHI 660E electrochemical station (CH Instruments, USA) with a three-electrode electrochemical cell, using a carbon rod and saturated calomel electrode (SCE) as the counter and reference electrodes, respectively. 1 M KOH solution (pH = 14) or 1 M KOH was used as electrolyte. All potentials of the electrochemical tests were performed as follows:

$E_{RHE} = E_{SCE} + 0.245 + 0.059 \times pH$ (V).

Before going on the test, high-purity Ar gas was bubbled through the solution for at least 30 min. The LSV curves, unless otherwise specified, were recorded at a scan rate of 5 mV·s^{-1} until the CV curves were stable without iR-compensation in different electrolytes. The C_{dl} measured with CV

curves, at a potential window between 0.07 and 0.12 V versus RHE, was performed with different scan rates from 15 to 40 $mV \cdot s^{-1}$. Based on the LSV curves, the Tafel plots were obtained by potential against log(current density). The EIS was recorded in the frequency ranging from 10^5 to 0.01 Hz at a 5 mV AC amplitude.

2. 3 DFT calculation

First-principle calculations were performed with using the Vienna *ab initio* simulation package (VASP), by which the geometric structures of all systems were relaxed and the energies were obtained correspondingly[28, 29]. The interaction between the electrons and ions was characterized by the method of projector augmented wave (PAW)[30]. Electronic exchange and correlation interactions were described by the functional of generalized gradient approximation (GGA) in the form of Perdew-Burke-Ernzerhof (PBE)[31]. We expanded the Kohn-Sham orbitals by plane waves with a kinetic energy cutoff of 550 eV. The Monkhorst-Pack meshes of Brillouin zone is 4×4×1. The force and energy criteria on each atom are −0.05 eV/Å and 10^{-5} eV, respectively. The Ru occupied in Ni(200) and Ni(111) surfaces were modeled by supercells. A vacuum layer was added to eliminate the interactions of two neighboring supercells along the *z*-axis.

2. 4 Synthesis of the complexes

Polyvinylpyrrolidone (PVP, M_w = 40000) and ruthenium trichloride ($RuCl_3 \cdot xH_2O$, 99%, 37.5～41 wt% Ru) were purchased from Adamas Reagent Co. Ltd. China. Nickel nitrate hexahydrate ($Ni(NO_3)_2 \cdot 6H_2O$, ≥ 98.0%), trimesic acid (H_3BTC, A.R.), N,N-dimethylformamide (DMF, A.R.) and ethanol (C_2H_5OH, A.R.) were bought from Sinopharm Chemical Reagent Co. Ltd. China. All chemicals were used without further purification.

2. 4. 1 Hollow spherical Ni-MOFs

The hollow spherical Ni-MOF was synthesized under solvothermal conditions. Typically, 216 mg of $Ni(NO_3)_2 \cdot 6H_2O$, 750 mg of PVP and 75 mg of H_3BTC were dissolved in 15 mL of a solution containing water, ethanol and DMF (The volume ratio is equal to 1/1/1). After vigorous stirring for 40 min, the uniform light green solution was transferred into a 30 mL Teflon-lined stainless-steel autoclave and heated to 150 ℃ for 16 h. The green products were collected by centrifugation at 4000 rpm for 10 min, washed with ethanol for 3 times and dried at 60 ℃ for 8 h, giving hollow spherical Ni-MOF.

2. 4. 2 Solid spherical Ni-MOFs

The solid spherical Ni-MOF was synthesized by using similar procedures with hollow spherical Ni-MOF, except for reducing the solvothermal reaction time to 3 h.

2. 4. 3 Hollow spherical NiRu-C nanohybrid

The hollow spherical NiRu-C nanohybrid was synthesized by using Ru^{3+}-doped Ni-MOF as the precursor. Firstly, the as-synthesized hollow spherical Ni-MOF was immersed into the ethanol solution containing different amounts of $RuCl_3 \cdot xH_2O$ for 12 h. Then the impregnated Ni-MOF was dried at 40 ℃ for several hours, obtaining Ru^{3+}-doped Ni-MOF. Finally, the hollow spherical NiRu-C nanohybrid was prepared by pyrolyzing the Ru^{3+}-doped Ni-MOF at 600 ℃ for 1 h at a heating rate of 2 $℃ \cdot min^{-1}$ under Ar atmosphere. For simplicity, the obtained samples prepared with 0.04, 0.06 and 0.08 g $RuCl_3 \cdot xH_2O$ were labeled as $NiRu_{0.04}$-C, $NiRu_{0.06}$-C and $NiRu_{0.08}$-C, respectively.

3 RESULTS AND DISCUSSION

Fig. 1 shows the schematic illustration for the preparation of hierarchical hollow spherical $NiRu_{0.06}$-C nanohybrid. Firstly, the hollow spherical Ni-MOF was solvothermally synthesized, during which the initially solid spherical Ni-MOF particles with smooth surface were gradually transformed into the hollow ones with uniform rod-like bulges on the surface[32]. The growth mechanism can be explained by Ostwald ripening, where the inner substance of the solid spheres dissolved and diffused to the surface, forming the hollow interior and generating rod-like bulges on the exterior with the prolonged reaction time. Then, the hollow spherical Ni-MOF was impregnated in an aqueous solution of $RuCl_3 \cdot xH_2O$ to obtain the hollow spherical Ru^{3+}-doped Ni-MOF. The powder X-ray diffraction (PXRD) patterns of both Ni-MOF and Ru^{3+}-doped Ni-MOF show similar characteristic peaks, which suggests that the incorporation of Ru^{3+} has no influence on the crystalline structure of the Ni-MOF (Fig. 2). The typical scanning electron microscopy (SEM) image of Ru^{3+}-doped Ni-MOFs in Fig. 3a also reveals its similar hollow spherical nanostructure to that of parent Ni-MOF. Finally, the Ru^{3+}-doped Ni-MOF was pyrolyzed in an Ar atmosphere to *in situ* synthesize the hierarchical hollow $NiRu_{0.06}$-C nanohybrid, during which the Ni and Ru atoms joined to form NiRu alloy NPs that homogeneously dispersed onto the hierarchical hollow carbon shells.

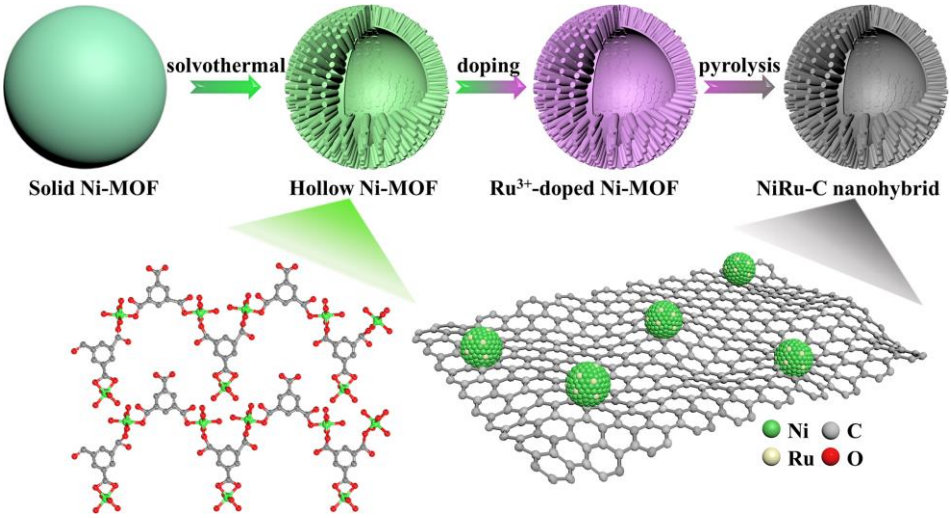

Fig. 1. Schematic illustration for the preparation of hierarchical hollow $NiRu_{0.06}$-C nanohybrid

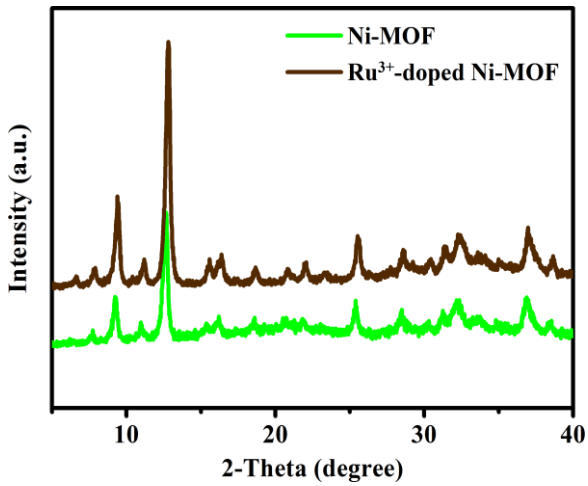

Fig. 2. PXRD patterns of hollow spherical Ni-MOF and Ru^{3+}-doped Ni-MOF

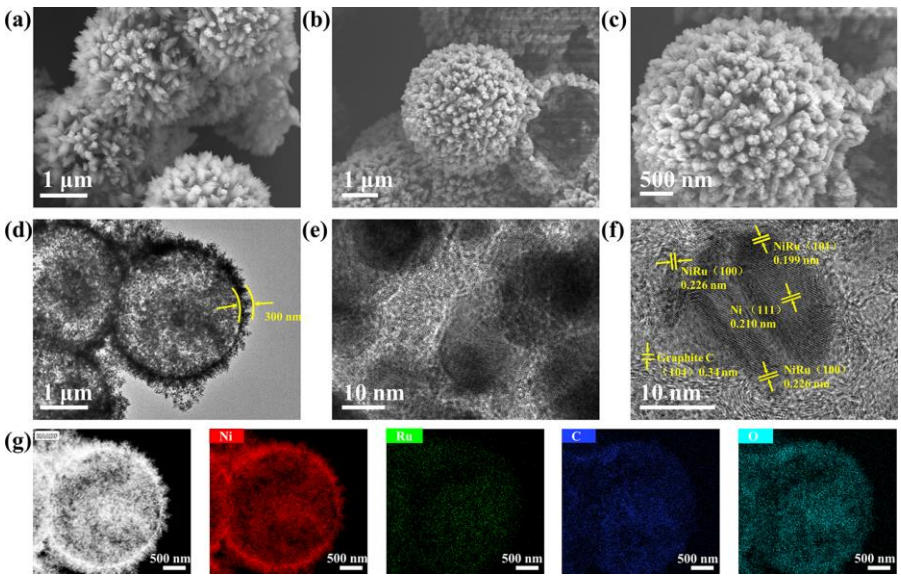

Fig. 3. SEM images of (a) hollow spherical Ru^{3+}-doped Ni-MOF; (b, c) SEM, (d, e) TEM and (f) HRTEM images of hollow spherical $NiRu_{0.06}$-C nanohybrid; (g) HAADF-STEM and corresponding element mapping images of $NiRu_{0.06}$-C for Ni, Ru, C and O elements

The SEM images of the as-prepared $NiRu_{0.06}$-C nanohybrid are shown in Figs. 3b～3c. As it can be seen, the $NiRu_{0.06}$-C nanohybrid derived from the Ru^{3+}-doped Ni-MOF can well maintain the hollow spherical nanostructure, where there are closely packed rod-like bulges on the surface. The transmission electron microscopy (TEM) images further attested the hollow spherical nanostructure of the $NiRu_{0.06}$-C nanohybrid with rod-like bulges on the exterior (Fig. 3d). The average length of the bulges was about 300 nm. The magnified TEM image of the hollow shell in Fig. 3e unambiguously revealed the distribution of crystalline RuNi alloy NPs over the carbon layer, as evidenced by the energy-dispersive X-ray (EDX) analysis (Fig. 4).

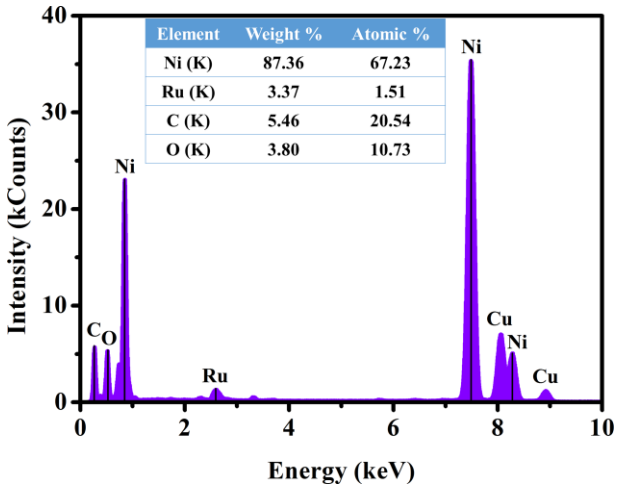

Fig. 4. EDX analysis of the $NiRu_{0.06}$-C nanohybrid

The crystalline structure of the NiRu alloy NPs was clearly identified in high-resolution TEM (HRTEM) image (Fig. 3f), in which, besides the looming lattice fringes of graphitic carbon with the interlayer distance of 0.34 nm, the lattice fringes with spacing of 0.199 and 0.226 nm near the edge are closely to the (101) and (100) planes of NiRu alloy. In addition, the lattice fringes with spacing of 0.210 nm attributed to the (111) plane of the cubic Ni can also be clearly observed. The contents of Ni and Ru in the $NiRu_{0.06}$-C nanohybrid were determined to be 66.41 and 2.67 wt% by the inductively coupled plasma atomic emission spectrometer (ICP-AES), which is consistent with the EDX result. Moreover, the high-angle annular dark-field scanning TEM (HAADF-STEM) and the corresponding element mapping are shown in Fig. 3g, confirming the homogeneous distribution of Ni and Ru elements throughout the hollow spherical nanostructure of the $NiRu_{0.06}$-C nanohybrid.

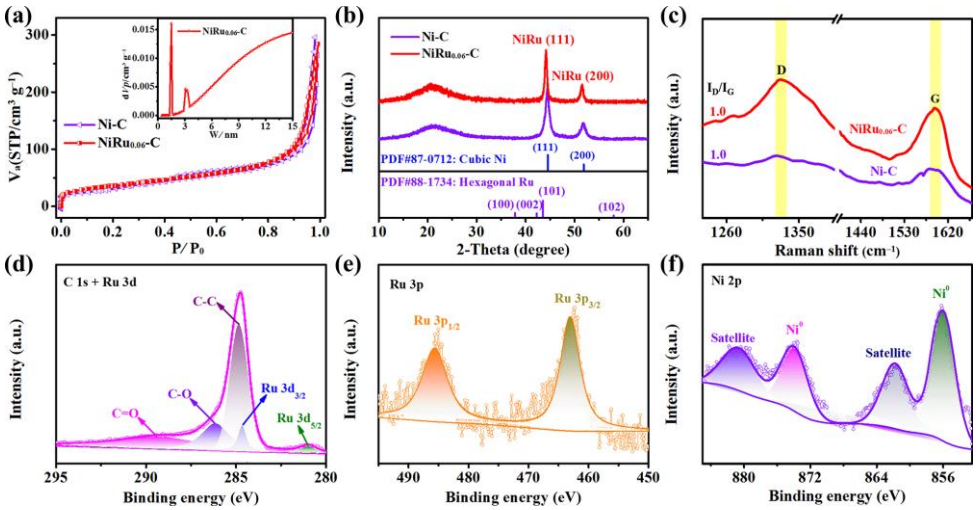

Fig. 5. (a) N_2 sorption isotherms and corresponding pore size distribution; (b) PXRD and (c) Raman spectra of $NiRu_{0.06}$-C and Ni-C; High-resolution (d) C 1*s* + Ru 3*d*, (e) Ru 3*p* and (f) Ni 2*p* spectra of $NiRu_{0.06}$-C

The specific surface and porosity of the hierarchical hollow spherical $NiRu_{0.06}$-C nanohybrid were investigated by the Brunauer-Emmett-Teller (BET) method. As shown in Fig. 5a, similar I/IV-type isotherms with high N_2 absorption and characteristic hysteresis loop at higher pressure verified the hierarchically porous structures of both hollow spherical $NiRu_{0.06}$-C and Ni-C. The obvious mesopores and micropores with a sharp peak in aperture distribution at about 1.1 and 3.8 nm can be observed over the $NiRu_{0.06}$-C nanohybrid (in the inset). Benefited from the distributed abundant micropores and mesopores within the shells, as well as the macropores between the closely packed bulges, the $NiRu_{0.06}$-C nanohybrid exhibits a BET surface area of 136.71 $m^2 \cdot g^{-1}$ and a pore volume of 0.42 $cm^3 \cdot g^{-1}$, which are similar with those of the Ni-C sample (142.38 $m^2 \cdot g^{-1}$ and 0.45 $cm^3 \cdot g^{-1}$). Furthermore, the crystalline structure of the $NiRu_{0.06}$-C nanohybrid was characterized by the PXRD analysis. As shown in Fig. 5b, besides the diffraction peak of graphite carbon at about 21.0 º, all the peaks of $NiRu_{0.06}$-C can be attributed to the cubic Ni, which suggests that the NiRu alloy keeps the crystalline structure of metallic Ni, as evidenced by the TEM analysis. While a slight shift to lower diffraction angle was observed for $NiRu_{0.06}$-C when compared with those of the Ni-C sample, implying the slight lattice expansion caused by the Ru atoms entered into the Ni lattices. In addition, the Raman spectrum of $NiRu_{0.06}$-C nanohybrid shows obvious D band (1327 cm^{-1}) and G band (1594 cm^{-1}), which are corresponding to the sp^3-type disordered carbon with edge plane defects and the defect-free sp^2-type graphitized carbon, respectively (Fig. 5c). The same intensity ratio of D and G bands (I_D/I_G) for $NiRu_{0.06}$-C and Ni-C suggests that the formation of NiRu alloy does not distinctly disturb the structure of the graphitic carbon. Moreover, X-ray photoelectron spectroscopy (XPS) was performed to investigate the electronic structure and chemical state of the $NiRu_{0.06}$-C nanohybrid. The survey spectrum in Fig. 6a confirms the existence of Ni, Ru, C and O elements in the $NiRu_{0.06}$-C nanohybrid. The high-resolution C 1*s* spectrum mixed with the Ru 3*d* spectrum in Fig. 5d can be accorded with C-C, C-O and C=O of graphitic carbon. The further high-resolution Ru 3*p* spectrum of $NiRu_{0.06}$-C with the binding energies at 485.6 and 463.0 eV are attributed to the Ru $3p_{1/2}$ and Ru $3p_{3/2}$ of Ru^0 (Fig. 5e). The high-resolution Ni 2*p* spectrum of $NiRu_{0.06}$-C in Fig. 5f exhibits the characteristic peaks of Ni^0 with the binding energies at 856.2 and 874.1 eV for Ni $2p_{1/2}$ and Ni $2p_{3/2}$, respectively. No metal-O bonding signal can be observed in the high-resolution O 1*s* spectrum (Fig. 6b). These results verify the successful formation of bimetallic NiRu alloy and graphitic carbon support through doping Ru^{3+} into Ni-MOF followed by pyrolysis treatment.

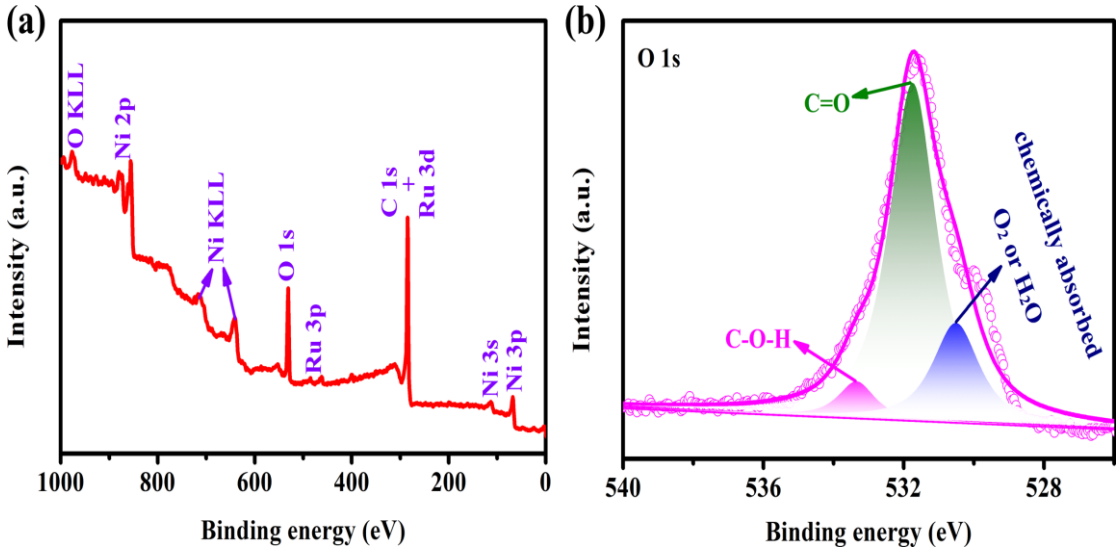

Fig. 6. (a) Survey spectrum of the $NiRu_{0.06}$-C nanohybrid; (b) High-resolution O 1*s* spectrum of the $NiRu_{0.06}$-C nanohybrid

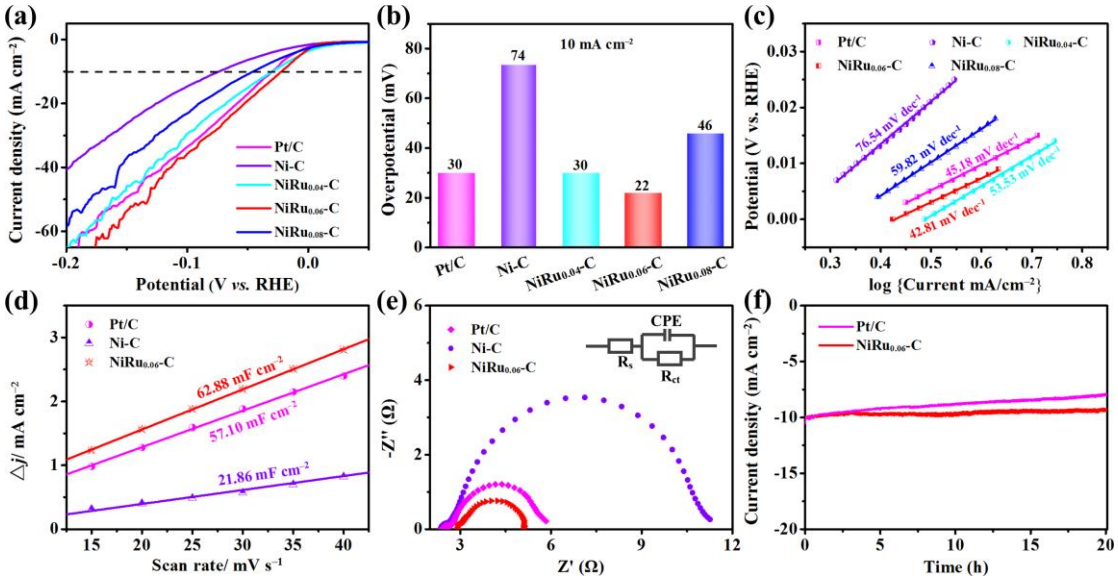

Fig. 7. HER performance of the $NiRu_{0.06}$-C nanohybrid and compared samples: (a) LSV plots, (b) Corresponding overpotentials at 10 mA·cm^{-2}, (c) Tafel plots, (d) Current density differences *vs.* scan rates and corresponding yielded C_{dl}, (e) EIS plots and (f) Chronoamperometric measurement

Inspired by the unique hierarchical hollow spherical nanostructure with rod-like bulges on the surface, the electrocatalytic performance of the $NiRu_{0.06}$-C nanohybrid for HER was evaluated in 1.0 M KOH in a typical three-electrode system, where the carbon rod and saturated calomel electrode (SCE) were used as the counter and reference electrodes, respectively. For comparison, the commercial 20 wt% Pt/C, the hollow spherical Ni-C and the $NiRu_x$-C nanohybrids with different Ru contents were also tested under the same conditions. All the electrochemical potentials were calibrated versus reversible hydrogen electrode (*vs.* RHE). As shown in Fig. 7a, the current density of $NiRu_{0.06}$-C was more negatively shifted compared with other compared samples, showing the excellent electrocatalytic activity for HER. The overpotential at 10 mA·cm^{-2} for $NiRu_{0.06}$-C is only 22 mV, which is far better than those of Pt/C (30 mV), Ni-C (74 mV), $NiRu_{0.04}$-C (30 mV) and $NiRu_{0.08}$-C (46 mV), respectively (Fig. 7b). Even when compared with the recently reported electrocatalysts for alkaline HER, the fairly lower overpotential of $NiRu_{0.06}$-C ranks it among the top few (Table 1). Furthermore, the outstanding HER performance of $NiRu_{0.06}$-C was confirmed by its smaller Tafel slope (42.81 mV·dec^{-1}) than those of Pt/C (45.18 mV·dec^{-1}), Ni-C (76.54 mV·dec^{-1}), $NiRu_{0.04}$-C (53.53 mV·dec^{-1}) and $NiRu_{0.08}$-C (59.82 mV·dec^{-1}), elucidating its favorable HER kinetics (Fig. 7c).

Table 1. Comparison of Selected Recently Reported Representative HER Electrocatalysts

Catalysts	Overpotential (mV) @10 mA·cm^{-2}	Electrolyte	Reference
$NiRu_{0.06}$-C	22	1.0 M KOH	This work
Pt/C	30	1.0 M KOH	This work
NiRu nanoalloys	32	1.0 M KOH	Ref. [33]
RuNi/CQDs	13	1.0 M KOH	Ref. [34]
Ru@CN	50	1.0 M KOH	Ref. [35]
Ru/NC-0.01	17	1.0 M KOH	Ref. [36]
Ru-NC-700	12	1.0 M KOH	Ref. [37]
Ru-MoO_2	29	1.0 M KOH	Ref. [38]
Ru@GnP	22	1.0 M KOH	Ref. [39]
NiFeRu-LDH	29	1.0 M KOH	Ref. [40]
RuP_2@NPC	52	1.0 M KOH	Ref. [41]
Ru@C_2N	17	1.0 M KOH	Ref. [42]

To probe the origin of the superior HER activity over the hierarchical hollow spherical $NiRu_{0.06}$-C nanohybrid, the electrochemically active surface areas (ECSA) that are in direct proportion to the double layer capacitance (C_{dl}) were evaluated by the test of cyclic voltammetry (CV) in the non-faradaic potential region (Figs. 7d and 8). The calculated C_{dl} value of $NiRu_{0.06}$-C is 62.88 mF·cm^{-2}, much larger than those of Pt/C (57.10 mF·cm^{-2}) and Ni-C (21.86 mF·cm^{-2}), implying that the NiRu alloy can provide more accessible active sites for electrocatalysis owing to the formation of hierarchical hollow nanostructure and high distribution of the active species. Furthermore, the catalytic kinetic of $NiRu_{0.06}$-C was also estimated by electrochemical impedance spectroscopy (EIS). As shown in Fig. 7e, the smallest charge transfer resistance (R_{ct}) of $NiRu_{0.06}$-C indicates the rapid electron/proton transfer at the interfaces of the catalyst and electrolyte, which can facilitate the catalytic process and thus bring an excellent HER activity. Moreover, the macropores between the closely packed bulges and the hollow structure can serve as the buffering reservoirs where the electrolyte can shorten the diffusion distances and easily diffuse into the mesopores and micropores of $NiRu_{0.06}$-C, thus greatly accelerating the mass transport during HER. Therefore, it can be logically deduced that the excellent HER activity of $NiRu_{0.06}$-C is attributed to the more exposed active sites in the nanohybrids and the efficient electron/mass transport in the unique hierarchical hollow spherical nanostructure with rod-like bulges on the surface.

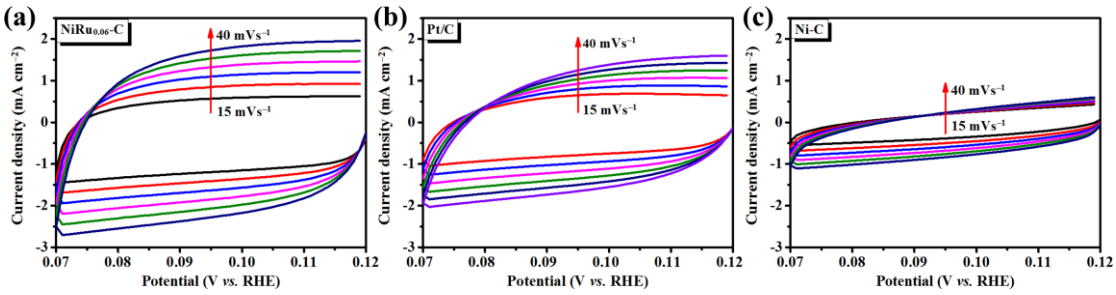

Fig. 8. CV curves of (a) $NiRu_{0.06}$-C, (b) Pt/C and (c) Ni-C between 0.07 and 0.12 V *vs.* RHE with an increasing scan rate of 5 mV·s^{-1} in 1.0 M KOH. The CVs of all samples exhibit the typical rectangular shapes of electrical double layer capacitors and the currents originate solely from electrical double layer charging and discharging

Besides, the stability of $NiRu_{0.06}$-C nanohybrid plays an important role in the evaluation of its catalytic performance. As shown in Fig. 7f, after the long-term stability tests for 80,000 s at an overpotential of 22 mV, $NiRu_{0.06}$-C maintained much better activity as compared to Pt/C. In addition, the hierarchical hollow spherical nanostructure of $NiRu_{0.06}$-C with rod-like bulges was well preserved after the chronoamperometric measurement (Fig. 9a). The PXRD analysis showed no significant crystalline change for $NiRu_{0.06}$-C before and after the chronoamperometric measurement (Fig. 9b). These results further confirm the excellent electrocatalytic stability of the $NiRu_{0.06}$-C nanohybrid.

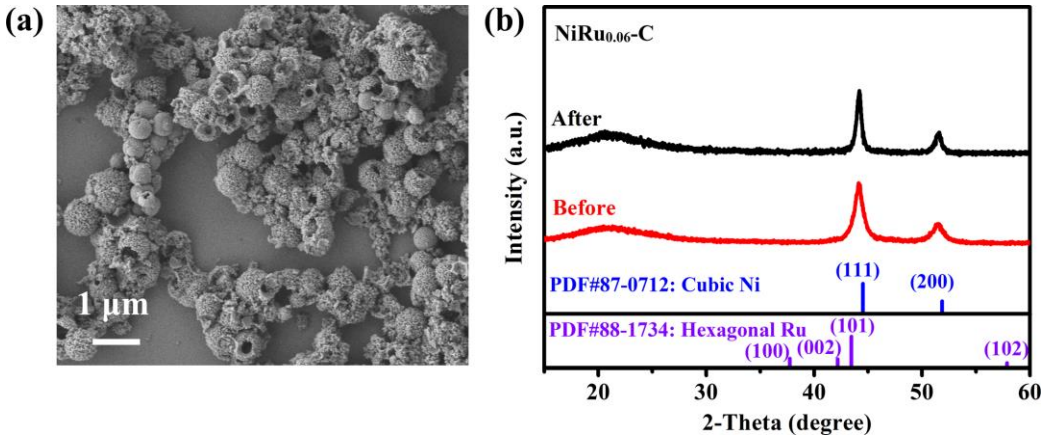

Fig. 9. (a) SEM images of the $NiRu_{0.06}$-C nanohybrid after the chronoamperometric measurement; (b) PXRD patterns of the $NiRu_{0.06}$-C nanohybrid before and after chronoamperometric measurement

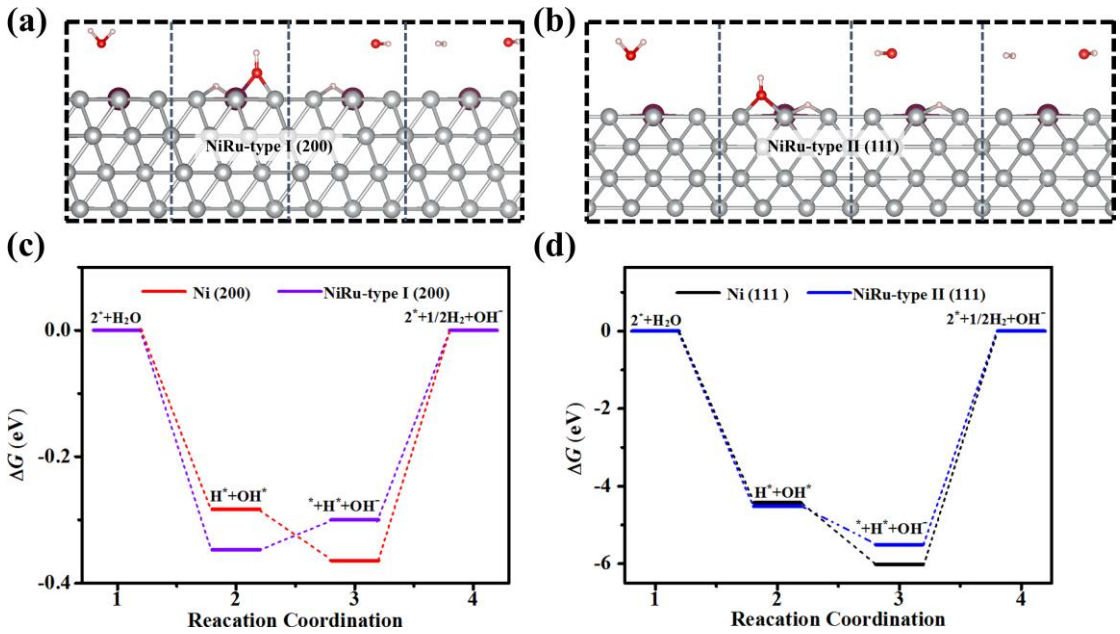

Fig. 10. Atomic configurations of the intermediates on the surface of (a) NiRu-type I (200) and (b) NiRu-type II (111). Light gray, dark purple, red and white represents the Ni, Ru, O and H atoms, respectively. The free energy diagrams over (c) NiRu-type I (200) and Ni (200), (d) NiRu-type II (111) and Ni (111) during alkaline HER reaction

To reveal the underlying mechanism for the outstanding HER activity of $NiRu_{0.06}$-C, DFT calculations were peformed. From the PXRD analysis of $NiRu_{0.06}$-C, the NiRu alloy should present the Ni (200) and Ni (111) planes as the dominantly observed surface. Thus, the NiRu-type I (200) with Ru doping in Ni (200) surface and NiRu-type II (111) with Ru doping in Ni (111) surface were modeled to represent the NiRu alloy in $NiRu_{0.06}$-C. Based on the experimentally measured Tafel slope values, the alkaline HER reaction over $NiRu_{0.06}$-C follows more likely the Volmer-Heyrovsky step, which includes the dissociation of H_2O to form the surface-bonded H^* and OH^*, the desorption of OH^* to release the surface sites and finally the desorption of H^* to generate gaseous H_2. The atomic configurations of the intermediates during HER on the modeled surfaces are shown in Figs. 10a and b. The corresponding free energy diagrams over the Ni surfaces with and without the Ru doping were also calculated. As shown in Fig. 10c, the energy barrier for the desorption of H^* can be obviously reduced over NiRu-type I (200) with Ru doping compared to the prinstine Ni (200). Similar enhancement effect derived from the Ru doping can also be observed over NiRu-type II (111) (Fig. 10d). Although the further comparison in Fig. 11 indicates that the prinstine Ni (200) and NiRu-type I (200) surfaces are more active than the prinstine Ni (111) and NiRu-type II (111) surfaces for the alkaline HER reaction, the desorption of H^* over both Ru-doped surfaces are thermodynamically favourable due to the decreased energy barrier, which can lead to the superior HER activity of $NiRu_{0.06}$-C than that of Ni-C, well consistent with the experimental demonstration.

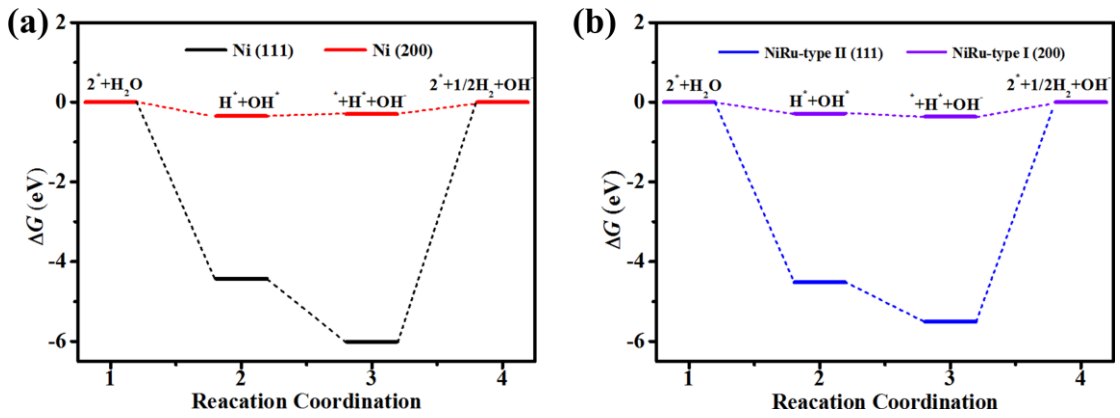

Fig. 11. Free energy diagrams over (a) Ni (200) and Ni (111), (b) NiRu-type I (200) and NiRu-type II (111) during alkaline HER reaction

4 CONCLUSION

To sum up, we report a scalable MOF-assisted strategy to synthesize the hierarchical hollow spherical NiRu-C nanohybrid with closely packed rod-like bulges on the surface. Benefited from the exposed active sites of NiRu alloy with high intrinsic activity and the efficient electron/mass transport in the unique hierarchical hollow spherical nanostructure, the optimized $NiRu_{0.06}$-C nanohybrid showed excellent performance for alkaline HER with ultralow overpotentials, which are superior to those of Pt/C and the majority of reported electrocatalysts. Our research may provide a guidance for the development of advanced electrocatalysts with controlled morphology and excellent performance for future energy applications.

REFERENCES

(1) Yang, Y.; Zhang, K.; Lin, H.; Li, X.; Chan, H. C.; Yang, L.; Gao, Q. MoS_2-Ni_3S_2 heteronanorods as efficient and stable bifunctional electrocatalysts for overall water splitting. *ACS Catal*. **2017**, 7, 2357−2366.

(2) Du, N.; Wang, C.; Wang, X.; Lin, Y.; Jiang, J.; Xiong, Y. Trimetallic tristar nanostructures: tuning electronic and surface structures for enhanced electrocatalytic hydrogen evolution. *Adv. Mater.* **2016**, 28, 2077–84.

(3) Ito, Y.; Cong, W.; Fujita, T.; Tang, Z.; Chen, M. High catalytic activity of nitrogen and sulfur co-doped nanoporous graphene in the hydrogen evolution reaction. *Angew. Chem. Int. Ed.* **2015**, 54, 2131–6.

(4) He, L.; Zhou, D.; Lin, Y.; Ge, R.; Hou, X.; Sun, X.; Zheng, C. Ultrarapid *in situ* synthesis of Cu_2S nanosheet arrays on copper foam with room-temperature-active iodine plasma for efficient and cost-effective oxygen evolution. *ACS Catal.* **2018**, 8, 3859–3864.

(5) Wan, C.; Regmi, Y. N.; Leonard, B. M. Multiple phases of molybdenum carbide as electrocatalysts for the hydrogen evolution reaction. *Angew. Chem. Int. Ed.* **2014**, 126, 6525–8.

(6) Tian, J.; Liu, Q.; Cheng, N.; Asiri, A. M.; Sun, X. Self-supported Cu_3P nanowire arrays as an integrated high-performance three-dimensional cathode for generating hydrogen from water. *Angew. Chem. Int. Ed.* **2014**, 53, 9577–81.

(7) Zheng, Y.; Jiao, Y.; Zhu, Y.; Li, L. H.; Han, Y.; Chen, Y.; Du, A.; Jaroniec, M.; Qiao, S. Z. Hydrogen evolution by a metal-free electrocatalyst. *Nat. Commun.* **2014**, 5, 3783.

(8) Li, L.; Wang, B.; Zhang, G.; Yang, G.; Yang, T.; Yang, S.; Yang, S. Electrochemically modifying the electronic structure of IrO_2 nanoparticles for overall electrochemical water splitting with extensive adaptability. *Adv. Energy Mater.* **2020**, 10, 2001600–9.

(9) Zheng, T.; Shang, C.; He, Z.; Wang, X.; Cao, C.; Li, H.; Si, R.; Pan, B.; Zhou, S.; Zeng, J. Intercalated iridium diselenide electrocatalysts for efficient pH-universal water splitting. *Angew. Chem. Int. Ed.* **2019**, 58, 14764–14769.

(10) Qin, F.; Zhao, Z.; Alam, M. K.; Ni, Y.; Robles-Hernandez, F.; Yu, L.; Chen, S.; Ren, Z.; Wang, Z.; Bao, J. Trimetallic NiFeMo for overall electrochemical water splitting with a low cell voltage. *ACS Energy Lett.* **2018**, 3, 546–554.

(11) Gupta, S.; Patel, M. K.; Miotello, A.; Patel, N. Metal boride-based catalysts for electrochemical water-splitting: a review. *Adv. Funct. Mater.* **2020**, 30, 1906481–28.

(12) Zhang, J.; Zhang, Q.; Feng, X. Support and interface effects in water-splitting electrocatalysts. *Adv. Mater.* **2019**, 31, 1808167–19.

(13) Han, X.; Tong, X.; Liu, X.; Chen, A.; Wen, X.; Yang, N.; Guo, X. Y. Hydrogen evolution reaction on hybrid catalysts of vertical MoS_2 nanosheets and hydrogenated graphene. *ACS Catal.* **2018**, 8, 1828–1836.

(14) Tang, Q.; Jiang, D. E. Mechanism of hydrogen evolution reaction on 1T-MoS_2 from first principles. *ACS Catal.***2016**, 6, 4953–4961.

(15) Bhalothia, D.; Huang, T. H.; Chang, C. W.; Lin, T. H.; Wu, S. C.; Wang, K. W.; Chen, T. Y. High-performance and stable hydrogen evolution reaction achieved by Pt trimer decoration on ultralow-metal loading bimetallic PtPd nanocatalysts. *ACS Appl. Energy Mater.* **2020**, 3, 11142–11152.

(16) Zou, X.; Zhang, Y. Noble metal-free hydrogen evolution catalysts for water splitting. *Chem. Soc. Rev.* **2015**, 44, 5148–80.

(17) Tao, Z.; Wang, T.; Wang, X.; Zheng, J.; Li, X. MOF-derived noble metal free catalysts for electrochemical water splitting. *ACS Appl. Mater. Interfaces* **2016**, 8, 35390–35397.

(18) Tang, Y. J.; Wang, Y.; Wang, X. L.; Li, S. L.; Huang, W.; Dong, L. Z.; Liu, C. H.; Li, Y. F.; Lan, Y. Q. Molybdenum disulfide/nitrogen-doped reduced graphene oxide nanocomposite with enlarged interlayer spacing for electrocatalytic hydrogen evolution. *Adv. Energy Mater.* **2016**, 6, 1600116–7.

(19) Marques Mota, F.; Choi, C. H.; Boppella, R.; Lee, J. E.; Kim, D. H. Arising synergetic and antagonistic effects in the design of Ni- and Ru-based water splitting electrocatalysts. *J. Mater. Chem. A* **2019**, 7, 639–646.

(20) Zhang, J. Y.; Tian, X.; He, T.; Zaman, S.; Miao, M.; Yan, Y.; Qi, K.; Dong, Z.; Liu, H.; Xia, B. Y. *In situ* formation of Ni_3Se_4 nanorod arrays as

versatile electrocatalysts for electrochemical oxidation reactions in hybrid water electrolysis. *J. Mater. Chem. A* **2018**, 6, 15653–15658.

(21) Li, C.; Liu, Y.; Zhuo, Z.; Ju, H.; Li, D.; Guo, Y.; Wu, X.; Li, H.; Zhai, T. Local charge distribution engineered by Schottky heterojunctions toward urea electrolysis. *Adv. Energy Mater.* **2018**, 8, 1801775–8.

(22) Chen, S.; Duan, J.; Vasileff, A.; Qiao, S. Z. Size fractionation of two-dimensional sub-nanometer thin manganese dioxide crystals towards superior urea electrocatalytic conversion. *Angew. Chem. Int. Ed.* **2016**, 55, 3804–8.

(23) Yuan, S.; Feng, L.; Wang, K.; Pang, J.; Bosch, M.; Lollar, C.; Sun, Y.; Qin, J.; Yang, X.; Zhang, P.; Wang, Q.; Zou, L.; Zhang, Y.; Zhang, L.; Fang, Y.; Li, J.; Zhou, H. C. Stable metal-organic frameworks: design, synthesis, and applications. *Adv. Mater.* **2018**, 30, 1704303–35.

(24) Cao, C.; Ma, D. D.; Xu, Q.; Wu, X. T.; Zhu, Q. L. Semisacrificial template growth of self-supporting MOF nanocomposite electrode for efficient electrocatalytic water oxidation. *Adv. Funct. Mater.* **2018**, 29, 1807418–8.

(25) Li, X.; Zhao, S.; Zhang, W.; Liu, Y.; Li, R. Ru nanoparticles supported on nitrogen-doped porous carbon derived from ZIF-8 as an efficient catalyst for the selective hydrogenation of *p*-chloronitrobenzene and *p*-bromonitrobenzene. *Dalton Trans.* **2016**, 45, 15595–15602.

(26) Yang, X.; Zhao, Z.; Yu, X.; Feng, L. Electrochemical hydrogen evolution reaction boosted by constructing Ru nanoparticles assembled as a shell over semimetal Te nanorod surfaces in acid electrolyte. *Chem. Commun.* **2019**, 55, 1490–1493.

(27) Li, W.; Liu, Y.; Wu, M.; Feng, X.; Redfern, S. A. T.; Shang, Y.; Yong, X.; Feng, T.; Wu, K.; Liu, Z.; Li, B.; Chen, Z.; Tse, J. S.; Lu, S.; Yang, B. Carbon-quantum-dots-loaded ruthenium nanoparticles as an efficient electrocatalyst for hydrogen production in alkaline media. *Adv. Mater.* **2018**, 30, 1800676–8.

(28) Kresse, G.; Hafner, J. *Ab initio* molecular dynamics for liquid metals. *Phys. Rev. B* **1993**, 47, 558–561.

(29) Kresse, G.; Furthmüller, J. Efficiency of *ab-initio* total energy calculations for metals and semiconductors using a plane-wave basis set. *Comput. Mater. Sci.* **1996**, 6, 15–50.

(30) Blochl, P. E. Projector augmented-wave method. *Phys. Rev. B* **1994**, 50, 17953–17979.

(31) Perdew, J. P.; Burke K.; Ernzerhof, M. Generalized gradient approximation made simple. *Phys. Rev. Lett.* **1996**, 77, 3865–3868.

(32) Bi, R.; Zeng, C.; Huang, H.; Wang, X.; Zhang, L. Metal-organic frameworks derived hollow NiS_2 spheres encased in graphene layers for enhanced sodium-ion storage. *J. Mater. Chem. A* **2018**, 6, 14077–14082.

(33) Xu, Y.; Yin, S.; Li, C.; Deng, K.; Xue, H.; Li, X.; Wang, H.; Wang, L. Low-ruthenium-content NiRu nanoalloys encapsulated in nitrogen-doped carbon as highly efficient and pH-universal electrocatalysts for the hydrogen evolution reaction. *J. Mater. Chem. A* **2018**, 6, 1376–1381.

(34) Liu, Y.; Li, X.; Zhang, Q.; Li, W.; Xie, Y.; Liu, H.; Shang, L.; Liu, Z.; Chen, Z.; Gu, L.; Tang, Z.; Zhang, T.; Lu, S. A general route to fabricate low-ruthenium-based bimetals electrocatalysts for pH-universal hydrogen evolution reaction via carbon quantum dots. *Angew. Chem. Int. Ed.* **2019**, 132, 1735–1743.

(35) Wang, J.; Wei, Z.; Mao, S.; Li, H.; Wang, Y. Highly uniform Ru nanoparticles over N-doped carbon: pH and temperature-universal hydrogen release from water reduction. *Energy & Environ. Sci.* **2018**, 11, 800–806.

(36) Liu, J.; Ding, G.; Yu, J.; Liu, X.; Zhang, X.; Guo, J.; Zhang, J.; Ren, W.; Che, R. Visualizing spatial potential and charge distribution in Ru/N-doped carbon electrocatalysts for superior hydrogen evolution reaction. *J. Mater. Chem. A* **2019**, 7, 18072–18080.

(37) Lu, B.; Guo, L.; Wu, F.; Peng, Y.; Lu, J. E.; Smart, T. J.; Wang, N.; Finfrock, Y. Z.; Morris, D.; Zhang, P.; Li, N.; Gao, P.; Ping, Y.; Chen, S. Ruthenium atomically dispersed in carbon outperforms platinum toward hydrogen evolution in alkaline media. *Nat. Commun.* **2019**, 10, 631–11.

(38) Jiang, P.; Yang, Y.; Shi, R.; Xia, G.; Chen, J.; Su, J.; Chen, Q. Pt-like electrocatalytic behavior of Ru-MoO_2 nanocomposites for the hydrogen evolution reaction. *J. Mater. Chem. A* **2017**, 5, 5475–5485.

(39) Li, F.; Han, G. F.; Noh, H. J.; Ahmad, I.; Jeon, I. Y.; Baek, J. B. Mechanochemically assisted synthesis of a Ru catalyst for hydrogen evolution with performance superior to Pt in both acidic and alkaline media. *Adv. Mater.* **2018**, 30, 1803676–7.

(40) Chen, G.; Wang, T.; Zhang, J.; Liu, P.; Sun, H.; Zhuang, X.; Chen, M.; Feng, X. Accelerated hydrogen evolution kinetics on NiFe-layered double hydroxide electrocatalysts by tailoring water dissociation active sites. *Adv. Mater.* **2018**, 30, 1706279–7.

(41) Pu, Z.; Amiinu, I. S.; Kou, Z.; Li, W.; Mu, S. RuP_2-based catalysts with platinum-like activity and higher durability for the hydrogen evolution reaction at all pH values. *Angew. Chem. Int. Ed.* **2017**, 129, 11717–11722.

(42) Mahmood, J.; Li, F.; Jung, S. M.; Okyay, M. S.; Ahmad, I.; Kim, S. J.; Park, N.; Jeong, H. Y.; Baek, J. B. An efficient and pH-universal ruthenium-based catalyst for the hydrogen evolution reaction. *Nat. Nanotechnol.* **2017**, 12, 441–446.